

Microchannel-Confined MXene Based Flexible Piezoresistive Multifunctional Micro-Force Sensor

Yuyu Gao, Cheng Yan, Haichao Huang, Tao Yang, Guo Tian, Da Xiong, Ningjun Chen, Xiang Chu, Shen Zhong, Weili Deng,* Yong Fang,* and Weiqing Yang*

Multifunctional micro-force sensing in one device is an urgent need for the higher integration of the smaller flexible electronic device toward wearable health-monitoring equipment, intelligent robotics, and efficient human–machine interface. Herein, a novel microchannel-confined MXene-based flexible piezoresistive sensor is demonstrated to simultaneously achieve multi-types micro-force sensing of pressure, sound, and acceleration. Benefiting from the synergistically confined effect of the fingerprint-microstructured channel and the accordion-microstructured MXene materials, the as-designed sensor remarkably endows a low detection limit of 9 Pa, a high sensitivity of 99.5 kPa⁻¹, and a fast response time of 4 ms, as well as non-attenuating durability over 10 000 cycles. Moreover, the fabricated sensor is multifunctionally capable of sensing sounds, micromotion, and acceleration in one device. Evidently, such a multifunctional sensing characteristic can highlight the bright prospect of the microchannel-confined MXene-based micro-force sensor for the higher integration of flexible electronics.

field is how to make these devices more versatile in the trend of greater integration and miniaturization. To overcome this challenge, combining functionally individual sensors into one composite structure to form a multi-functional sensor array^[4] is an effective strategy. However, it is becoming more and more difficult to integrate a plurality of independent devices with different functions into an increasingly space-limited device, which results in complicated operation and high price, conflicting with requirements of miniaturization and integration toward the microelectronic device. Alternatively, multifunctional sensing can be realized in one device through a smartly compact structure design.^[5] Typically, as a fundamental way for an object to interact with others, force detection can help us

1. Introduction

Microelectronic devices play a vital role in human healthcare monitoring,^[1] intelligent robotics,^[2] and human machine interface.^[3] One critical challenge commonly recognized in this

realize the multifunctional information sensing, such as pulse detecting,^[6] sounds recognition,^[7] and load weighting.^[8] To date, various mechanisms have been utilized for force sensing, such as piezoresistive,^[9] piezoelectric,^[10] triboelectric,^[11] and so on. Among them, flexible piezoresistive pressure sensors^[12] draw tremendous attention owing to its simple structure, feasible fabrication process, low energy consumption, easy signal processing, and high sensitivity. In recent years, flexible piezoresistive pressure sensors have been developed rapidly, mainly focusing on the structure design, such as lotus leaf,^[13] sandpaper^[14] and epidermis,^[15] and piezoresistive materials optimization, like retreatment leather,^[16] reduced graphene oxide wrapped polyvinylidene difluoride nanofiber film^[17] and carbonized silk nanofiber membrane.^[18] Particularly, MXenes^[19] (Ti₃C₂T_x), as a newly 2D early transition metal carbides or carbonitrides, is a new type of accordion-like laminated material that can be used as piezoresistive material. Its compressible sheets-laminated structure is a crucial factor to change the MXene internal resistance and the conductivity of the MXenes. Nevertheless, the present MXene based pressure sensor^[20] quickly reached the deformation limit of MXenes in limited space of the 2D plane under the external stimulation, which considerably restricts the sensor's performance. Additionally, most of the previous studies just focused on the sensitivity or limit of pressure detection or other indicators, while few of them could perceive the multifunctional microforce within one simple structure, like sounds, touch, and motion recognition.

Y. Gao, C. Yan, H. Huang, T. Yang, G. Tian, D. Xiong, N. Chen, X. Chu, S. Zhong, Dr. W. Deng
Key Laboratory of Advanced Technologies of Materials
(Ministry of Education)
School of Materials Science and Engineering
Southwest Jiaotong University
Chengdu 610031, P. R. China
E-mail: weili1812@swjtu.edu.cn

Prof. Y. Fang
Key Laboratory of Transportation Tunnel Engineering
Southwest Jiaotong University
Chengdu 610031, P. R. China
E-mail: fy980220@swjtu.edu.cn

Prof. W. Yang
Key Laboratory of Advanced Technologies of Materials
(Ministry of Education)
School of Materials Science and Engineering
State Key Laboratory of Traction Power
Southwest Jiaotong University
Chengdu 610031, P. R. China
E-mail: wqyang@swjtu.edu.cn

 The ORCID identification number(s) for the author(s) of this article can be found under <https://doi.org/10.1002/adfm.201909603>.

DOI: 10.1002/adfm.201909603

Herein, we demonstrated a novel microchannel-confined MXene based flexible multifunctional piezoresistive pressure sensor. Ascribing to the microchannel-confined effect of the fingerprint-structured channel, MXenes could be well confined in trenches and form a 3D stacked structure, which endows MXenes with larger deforming space and more sensitive micromotion ability. Combined with the fingerprint-microstructured channel and accordion-microstructured MXenes, both the distance between different MXenes and neighboring interlayers in MXenes will decrease to varying degrees as the external force changes, resulting in the similar changes of corresponding resistance. Profiting from this elastically confined effect, the as-developed piezoresistive pressure sensor exhibits a low detection limit of 9 Pa, a high sensitivity of 99.5 kPa⁻¹, a fast response time of 4 ms as well as great reproducibility over 10 000 cycles. More importantly, this pressure sensor could achieve multifunctional microforce sensing such as pressure, sound, acceleration, or even the micro-motions by the only one structure in one device, evidently making it possible to fabricate a flexible piezoresistive multifunctional micro-force sensor in a low-costly simple way.

2. Result and Discussions

Figure 1a schematically presents the multifunctional force sensing sensor toward sound wave monitoring, etc. This sensor can be mainly divided into three parts (Figure 1b), namely top Au electrode on plane poly ethylene terephthalate (PET) substrate, middle MXene layer, and bottom Au electrode on fingerprint-like circle array micro-structured PET substrate in sequence. The corresponding Au electrode was coated on the

film substrate by magnetron sputtering (Figure S1, Supporting Information), while MXene layer was dipped and dried on the micro-structured PET film to build a force sensitive layer, which was sandwiched between the above two Au electrodes. In order to effectively confine these discontinuously layered MXenes, the micro-channeled structure was rapidly etched by cold ultraviolet laser to construct fingerprint-like circle arrays with the internal distance of 80 μm (Figure S2, Supporting Information). This cold laser manufacturing process can effectively guarantee the smoothness and completeness of fingerprint-like microchannels, which was obviously proved by its cross-sectional images (Figure S3, Supporting Information). Furthermore, both vividly-ringed white interference images (Figure 1c) and periodically fluctuated contour line (upper right in Figure 1c) distinctly demonstrate the 3D structured and high-quality fingerprint-like features of micro-structured PET substrates. Subsequently, to further promote the stability and flexibility, two pieces of polyurethane (PU) films used as protective layers were attached to encapsulate the sensor inside, as shown in Figure S4, Supporting Information. Almost all fabrication procedures can be carried in an air and nontoxic environment, as briefly illustrated in Figure S5, Supporting Information, which exhibits gigantic potential for scalability production, such as a 9 × 9 pressure sensor array indicated in Figure 1d.

The excellent conductivity adjustability of MXenes with interlayer distance promises a naturally optimal piezoresistive material for the pressure sensor. Here, Ti₃C₂T_x MXenes (Figure 1e and Figure S6, Supporting Information) was obtained through selectively etching the element A from the parent phase MAX (Ti₃AlC₂). Its SEM image (the top right of Figure 1b) obviously verifies the multilayer-structured feature, while the X-ray diffraction pattern (Figure S7, Supporting Information) indicates

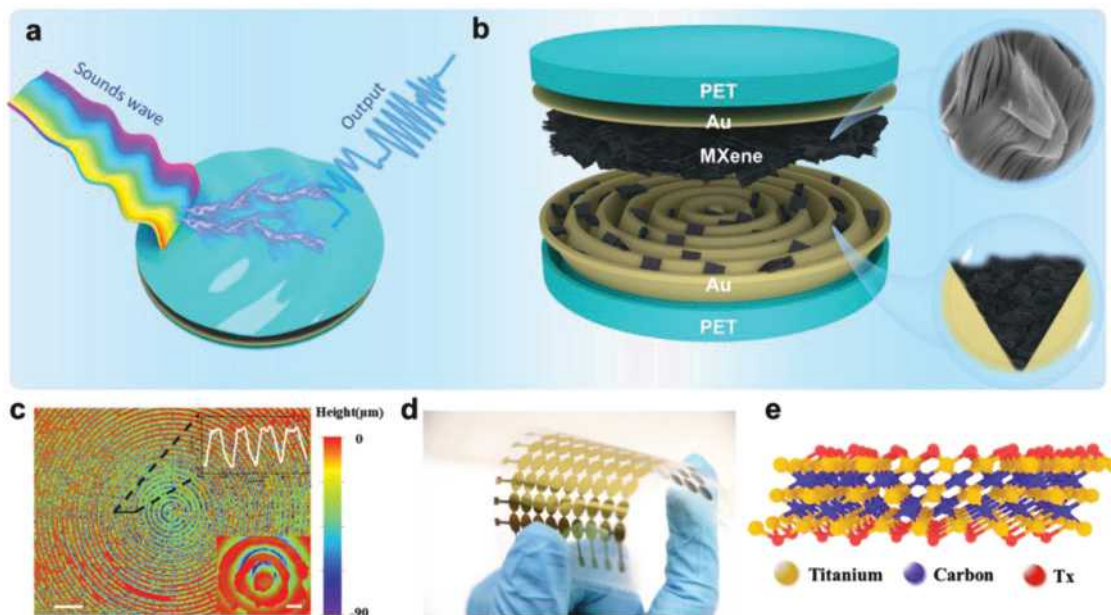


Figure 1. Schematic illustration of the pressure sensor. a) A beam of sound waves hit on the surface of the pressure sensor. b) The general illustration and detailed structure of the pressure sensor; Left: Structure of the pressure sensor; Upper right: SEM image of the accordion-like MXenes; Bottom right: Schematic of MXenes filled in the microchannel. c) 3D white light interference image of the fingerprint-like micro-channelled PET film. Inset: The enlarged 3D image. Respectively, the scalebars are 500 and 100 μm. d) Photograph of the flexible pressure sensor array. e) The molecular structure of the MXenes.

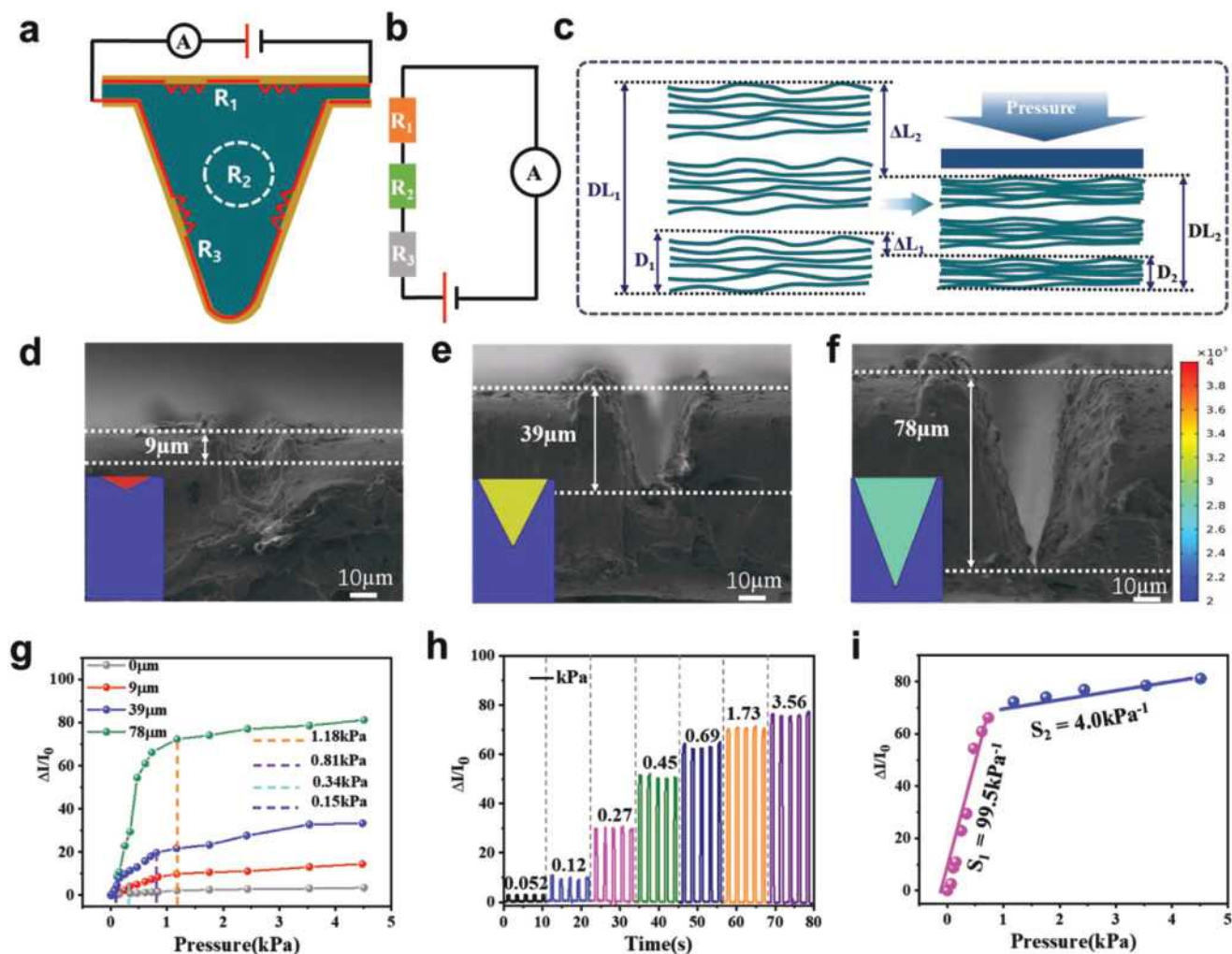


Figure 2. Working mechanism of the microchannel-confined MXene-based piezoresistive pressure sensor and the basic performance of the sensor. a) The equivalent resistance model of the as-prepared sensor. b) The equivalent circuit diagram of the pressure sensor. c) The thickness (D_1/D_2) of single MXenes and the wider distance (DL_1/DL_2) between MXenes decrease under an external pressure. d–f) SEM images of the laser engraved microstructure with the channels of 9, 39, 78 μm . Inset: FEA simulation of the stress state of MXenes in different depth channels under the same pressure. g) The electrical performance of the pressure sensors with various depth of the channels. h) Real-time current response of the pressure sensor with channel depth 78 μm under loading and unloading from 0.052 to 3.56 kPa. i) Sensitivity of the pressure sensor with channel depth 78 μm .

that most of Ti_3AlC_2 have successfully transformed to $\text{Ti}_3\text{C}_2\text{T}_x$. The more detailed characteristic information about MXenes can be found in Note S1, Supporting Information.

To further analyze the working mechanism of the device, an equivalent resistance model of this as-prepared sensor was established. The whole resistance consists of two parts, bulk resistance (R_2) of confined $\text{Ti}_3\text{C}_2\text{T}_x$ MXenes and interface resistances (R_1 and R_3) between MXenes and its adjacent electrodes, as shown in **Figure 2a**. And the corresponding electro circuit was illustrated in **Figure 2b**. As seen, the working principle of the device under external pressure was shown in **Figure 2c**. When pressure was applied, both the distance among the MXenes ($DL_1 \rightarrow DL_2$) and the space between the neighboring interlayers in MXenes ($D_1 \rightarrow D_2$) would decrease simultaneously, then the internal resistance R_2 reduced and the conductivity increased oppositely. Besides, the contact areas between MXenes and Au electrode were increasing simultaneously, which would bring

down the interface resistances (R_1 and R_3) and then enhance the current value. With the pressure further increasing, the limited spaces among MXenes are squeezed in a high degree and the distance between neighboring interlay sheets of the MXenes reduced slowly. Corresponding, the internal resistance R_2 and interface resistances (R_1 and R_3) decrease in a slow speed, resulting in a tough increase in conductivity.

To further verify the confinement effect generated by the micro-channel, three types of micro-structured PET films with the different channel depths were chosen to fabricate sensors for exploring the relationship between confined-degree and electrical performance. Before that, finite element analysis (FEA) was implemented to simulate the stress distribution of the confined MXenes in different depth channels. A simplified 2D FEA model was designed as shown in **Figure 2d–f**: the blue area represents the microstructured PET film and the inverted triangle area represents the MXenes powder. When

the same pressure is applied on the channel, it is obvious that the stress distribution of MXenes changes with the depth of the channel, the deeper channel, the smaller stress, which indicates that the MXenes in shallower channel would reach their deformation limitation more quickly. And the dependence relationship of MXenes stress on micro-channel depth was shown in Figure S8, Supporting Information, obviously indicating that the deeper the channel, the smaller the stress. When MXenes are confined in channels, the MXenes-between porous space makes them more deformable. Therefore, under the same pressure, the MXenes in the shallower channel more easily reach maximal deformation threshold. On the contrary, MXenes in deeper channels still have the margin to be compressed and deformed. Considering the above comprehensive analysis, the microchannel-confined effect ensures the controllability of the sensor performance by adjusting the depth of the channels.

Furthermore, the electrical performances of the as-fabricated sensor were studied with different channel depths of 0, 9, 39, and 78 μm under a constant voltage of 0.1 V. Here, the sensitivity (S) of the sensor is defined as $S = ((I - I_0)/I_0)/P$, where I is instantaneous current value when the sensor with load, I_0 is the initial current value without load and P is the applied pressure. The electrically measured results were illustrated in Figure 2g. It can be seen that all the sensors with different channel depths have the response to the external pressures, but under the same pressure, the deeper the channel, the larger the electrical output. Especially, stress in the deeper channel is comparatively smaller than the shallower one under the same pressure. Therefore, the MXenes in the deeper channel have a larger deformation capacity which endows a higher linearity range to the devices as shown in Figure 2g. Comprehensively chewing upon the structure strength and flexibility, the etched channel with a depth of 78 μm into PET film with a thickness of 100 μm was optimally selected as the ideal parameter for future experiments. Figure 2h exhibits the stable response of the pressure sensor under different pressure ranging from 0.05 to 3.5 kPa. This device shows a high sensitivity of 99.5 kPa^{-1} under the pressure less than 1 kPa and a relatively low sensitivity of 4.0 kPa^{-1} under the pressure from 1 to 4.5 kPa (Figure 2i), which is much higher than previous works^[3d,21] and other similar commercialized pressure sensor ($S = 0.24 \text{ kPa}^{-1}$, Figure S9, Supporting Information).

To further study the performance of the microchannel-confined MXene-based pressure sensor in detail, a series of measurements were carried out. First, masses of different weights were placed on the fabricated device to determine the lower detection limit of the sensor (Figure 3a). Even a tiny mass with a weight of 89 mg under a corresponding pressure of 9 Pa (Figure 3b) could be detected by this as-designed device, evidently presenting the excellent detection capability. In addition, this designed sensor also shows the fast response time of 4 ms and the recovery time of 13 ms, which ensures the feasibility of real-time multifunctional sensing (Figure 3c). To visualize the sensitivity of the applied pressure, a LED was connected in series with the sensor and a constant voltage of 3 V was applied. After placing bottles with different weight of ink (empty, half, full) one after another, the brightness of LED showed a significant change with the variety of the pressure value, as exhibited

in Figure 3d and Movie S1, Supporting Information. Besides, when stepped pressures, namely 0, 245, 383, 430, and 622 Pa, were gradually applied on the sensor, the corresponding current values remain well at the identical pressure during the loading–unloading process (Figure 3e), which further circumstantiated the real-time response of the as-fabricated piezoresistive sensor. Furthermore, the good linearity relationship of the current–voltage (I – V) curve (Figure 3f) from -1 to 1 V suggested that ohmic contacts were respectively formed between MXene and top, bottom electrodes. From the results, it also can be seen that the slope of the I – V curves decreased with the decrease of external pressure, which indicating the resistivity of the device can be continuously increased with the decreasing of external force. And all these results agreed well with theoretical analysis. Figure 3g is a graph of current versus pressure as the voltage is 0.1 V from Figure 3f, which shows the close sensitivity level in Figure 2g. In addition, to explore the reproducible sensing performance of the device, a constant pressure of 364 Pa was repeatedly loaded and unloaded on the sensor for over 10 000 times and there is no significant recession as shown in Figure 3h, indicating the remarkable robustness. Profiting from the simplicity of structure and easy fabrication process, a 9×9 sensor array was also made to show the ability for scalable applications. On this basis, several bottles with different weights of water were placed on the sensor array, as exhibited in the upper part of Figure 3i, which resulted in different heights of local pillars as depicted in the lower part of Figure 3i.

All of the above characterizations and analyses imply that this microchannel-confined MXene based pressure sensor has excellent sensing performance especially in the tiny pressure regime, and also enables the sensor with multi-functional detecting capabilities. For human activity monitoring, the fabricated piezoresistive sensor can be flexibly attached on the human throat and wrist (Figure 4a) to detect the human voice and wrist pulse. As indicated in Figure 4b, the sensor can record the current changes when speaking different words like “hello” and “sensor.” Clear distinction can be observed from recorded curves, “sensor” curve has two peaks while “hello” curve has only one because of different words have different syllables. It displays the ability to distinguish the different signals of the weak throat vibration, exhibiting a huge potential for voice recognition. Besides, the micro-channel confined MXene based pressure sensor could be also used for timely monitoring the physiological signal of the wrist pulse. As shown in Figure S10 and Movie S2, Supporting Information, a periodic and steady pulse signal reveals that the heart rate of the tested host is 68 $\text{beat} \cdot \text{min}^{-1}$. And the enlarged curve in Figure 4c legibly exhibits the typical peaks of human pulse waveform, namely P1 (Percussion), P2 (Tida), and P3 (Diastolic),^[22] which are the crucial information for monitoring cardiovascular disease.

Besides, acceleration is another important parameter for human–machine interface, smart robotics, etc. As the micro-channel confined MXene based pressure sensor being firmly attached on the vibration table (Figure 4d), the corresponding output signal was varying with the frequency at the same amplitude (Movie S3, Supporting Information). Then the acceleration can be acquired from the relationship between the frequency and acceleration (Figure S11, Supporting Information).

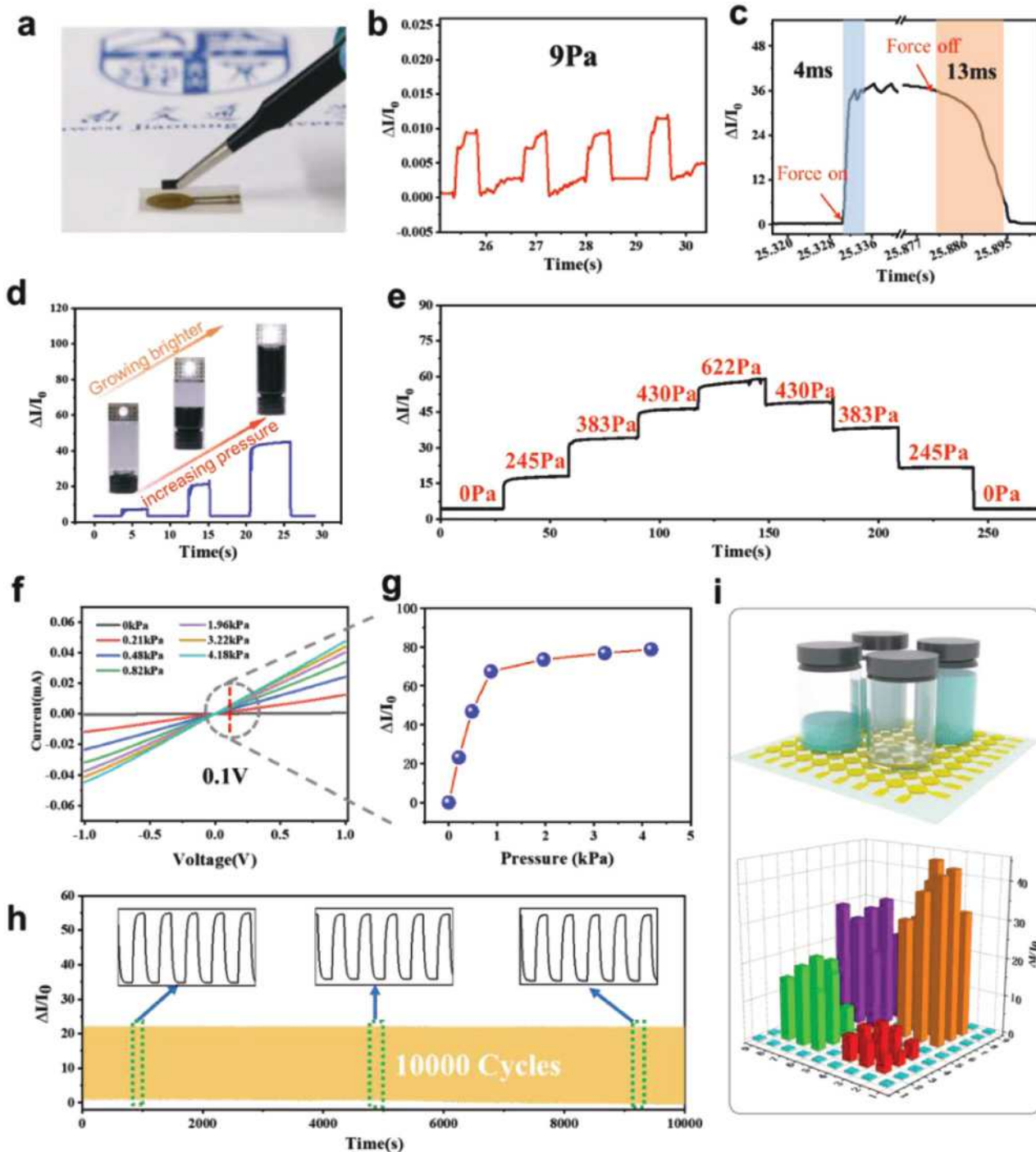


Figure 3. The electrical performance of the pressure sensor with channel depth of 78 μm . a) Photograph of putting a tiny mass on the pressure sensor. b) The pressure sensor can detect the tiny pressure as low as 9 Pa. c) Response time and recovery time of the pressure sensor. d) A bottle containing ink is placed on the pressure sensor which is in series with a LED. With the amount of ink increasing, the LED gets brighter. e) The current response under stepped pressure. f) I–V curves of the pressure sensor with various pressures. g) Current response with various pressures at 0.1 V bias voltage. h) The durability test under a pressure of 364 Pa. i) Four bottles filled with different degree of water were placed on 9×9 sensor array and the corresponding value mapping.

In addition, when the sensor was well fixed on a vibrating plate, it showed a highly sensitive performance for detecting the damping-like movement of the object as illustrated in Figure 4e and Movie S4, Supporting Information.

In detail, as explicated in Figure 4f,g, this whole detecting process can be divided into four stages through the relationship among the displacement, velocity, acceleration, and the corresponding current of the sensor. At stage i, the sensor is just

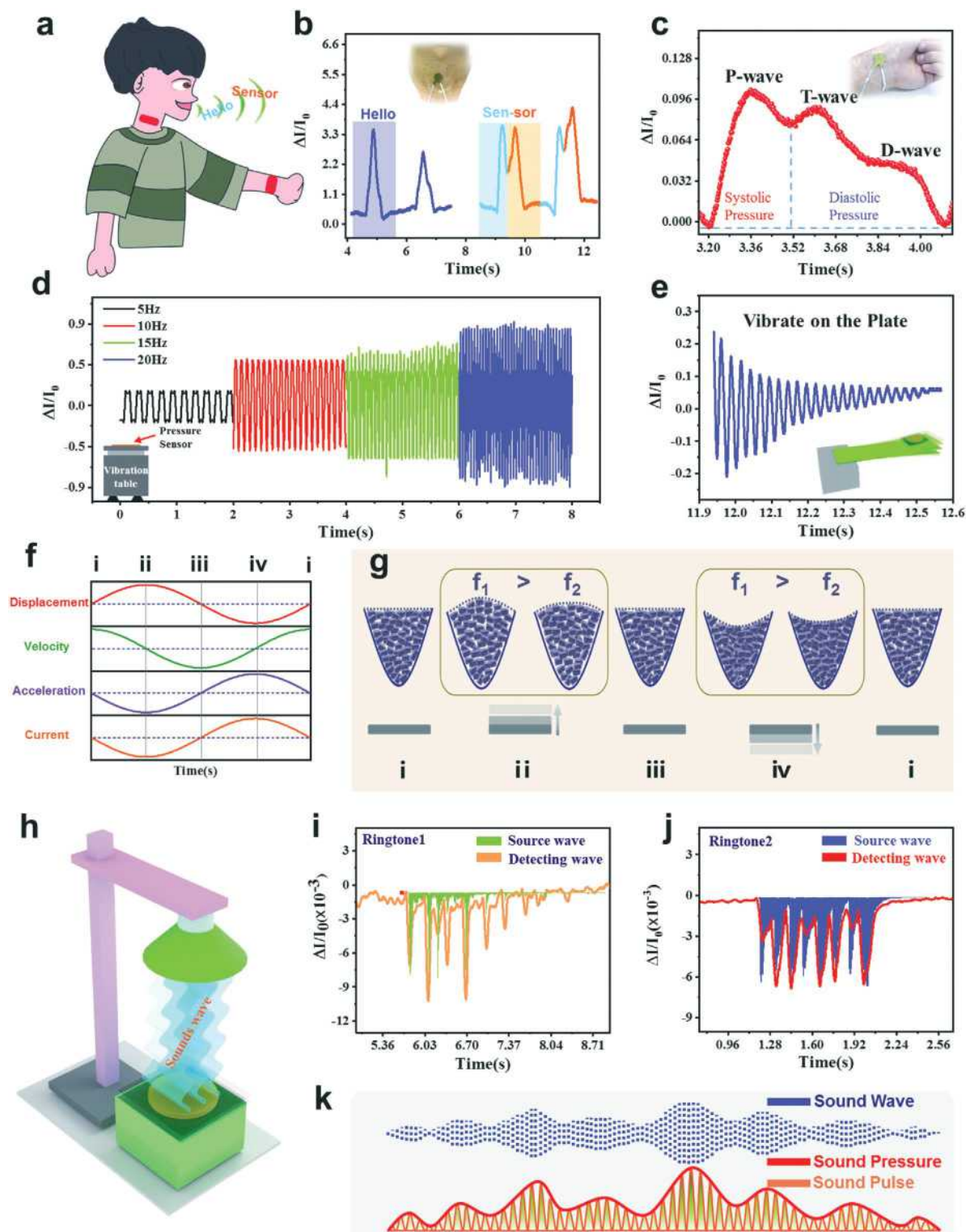


Figure 4. The application of the pressure sensor for tiny signal detection. a) Schematic illustration of the pressure sensor used as a wearable device for physiological signal detection. b) Corresponding signals for speaking “hello” and “sensor.” Inset: Photograph of the sensor attached on throat. c) Corresponding signals of wrist pulse. Inset: Photograph of the sensor attached on wrist. d) Corresponding signals of pressure sensor vibrating at different frequencies on vibrate table. e) Corresponding signals of the pressure sensor vibrating on plate. f) In vibrating mode, the relationship between corresponding current value, displacement, velocity, and acceleration. g) Schematic of the MXenes density on different stages of vibration. h) Schematic of the sounds wave hit on the pressure sensor. i) Illustration of the sound pressure on the surface of the sensor associated with the sounds wave and sounds pulse. j–k) Corresponding detected signals and source waves of two ringtones.

moving at the middle position of the vibration path and reaches its maximum velocity, the acceleration begins to increase in the downward direction and MXenes in sensor keep in a balanced position so that the current is also at the initial value. When reaching stage ii, the sensor stays at the top position of the vibration path while the downward acceleration reaches maximum which causes downward speed decreasing to zero. At the same time, MXenes in the sensor have an upward movement tendency under inertial effects, which causes MXenes in the channel to keep low density and resulting in the increase of MXenes resistance and the decrease of current. In stage ii, when $f_1 > f_2$, the density of MXenes at f_1 is lower than that of f_2 (f_1 and f_2 , respectively represent large and low acceleration). Then in stage iii, sensor returns to the middle position, downward speed reaches maximum, the acceleration reaches zero and current returns to initial value. After that, in stage iv, sensor at the bottom position, the velocity reaches zero and it is ready to increase in upward direction for the upward acceleration reaches the maximum. Owing to the inertial effect, the MXenes in channel tend to be downward, which will lead to the large density of the MXenes in channel, as a result, the resistance among particles decreases and the corresponding current increases. Finally, the sensor will go back to stage i and begin the next cycle. As can be seen, the designed micro-channel confined structure combined with conductive MXenes ensure the sensor not only has the ability to detect tiny pressure, but also can be used for detecting the acceleration of the object.

It is well known that sound waves are longitudinal waves and the propagation of sound waves is actually the movement of longitudinal pulse. Due to the excellent sensitivity, the micro-channel confined MXene based sensor was also been exploited for detecting sounds as shown in Figure 4h and the experiment system was illustrated in Figure S12, Supporting Information. Because the interaction between the sound waves and sensor surface is a series of air pulse caused by sound waves, and the pressure generated on the sensor surface is the average force caused by these pulses (Figure 4i), then the sound can be detected by the micro-force sensitive sensor. Based on the developed sensor, the corresponding signals of different ringtones can be detected. As illustrated in Figure 4j,k, the corresponding detecting signals (line graph) of different ringtones (color map) were respectively depicted and the detailed sounds can be found in Movie S5, Supporting Information. In comparison, the waveforms of the detected signals in both figures are basically consistent with the contour of the source waveform, especially the peaks can be completely corresponded, which exhibit excellent detection capability. However, when the sound source amplitude is too small, the detected signal will have some deviation. This is mainly because the signal with too small amplitude has exceeded the detection limit of the sensor. Even so, the above demonstrations confirmed the validity and the inspiring prospect of the microchannel-confined piezoresistive pressure sensor for multifunctional micro-force sensing.

3. Conclusion

In summary, a highly sensitive microchannel-confined MXene based flexible multifunctional piezoresistive pressure sensor

was developed by the designed channel confined effect and the compressible laminated MXene ($\text{Ti}_3\text{C}_2\text{T}_x$). This designed sensor not only achieves a low detection limit (<9 Pa), a high sensitivity (99.5 kPa^{-1}), and fast response (4 ms), but also can simultaneously realize the multifunctional microforce sensing such as detecting wrist pulse, sounds, micromotion, and even the acceleration of the host only in one device. Such multifunctional sensing characteristic leads the sensor a promising application in smaller flexible electronic devices toward the wearable healthcare monitoring equipment, intelligent robotics, and efficient human-machine interfaces.

4. Experimental Section

Preparation of the MXenes: The MXenes ($\text{Ti}_3\text{C}_2\text{T}_x$) was obtained by etching the commercial MAX (Ti_3AlC_2 , 11 Technology Co., Ltd., China) powder with HF (49% wt, MACKLIM Co., Ltd., China). And MAX (2 g) was slowly added into HF (20 mL), then stirred at 40 °C for 40 h to etch Al element. Subsequently, the resulted solution was centrifuged and washed several times until the pH reached around 6. The final sediment was dried at 45 °C for 24 h in vacuum oven.

Fabrication of the Electrode PET Film: The structured PET film (thickness: 100 μm) was fabricated by cold laser marking machine (UV-3S, China), the radius of the structured area was 5.6 mm and the adjacent spacing was 80 μm . Then Au electrode was coated on the film by magnetron sputtering equipment for 10 min. And the flat electrode PET film was obtained in the same way.

Preparation of the Microchannel Confined MXene Based Sensor: The MXene particles (0.125 g) were added into absolute ethyl alcohol (0.5 mL) and blended in vortex mixer for 2 min. Then the solution (50 μL) was transferred to the electrode area of the PET film, and the flat electrode was covered on it. After extracting the electrode by aluminum tape, the device was encapsulated by polyurethane films.

Characterization and Measurement: Surface morphology and compositions of the samples were characterized through SEM (FEI QUANTA FEG 250, American) and energy-dispersive X-ray spectroscopy (S4800). The surface 3D structure was obtained by BRUKER ContourGT. The phase identification of the samples was carried out by the X Pert Pro (Holland) X-ray diffract meter with $\text{Cu K}\alpha 1$ radiation ($\lambda = 0.154$ nm) from 5° to 90° . The current signals of the sensor were measured by the low-noise current preamplifier (Stanford Research SR570). Stepping motor and piezometer (IMADA-ZP) were used for pressure applying and durability test. The I-V relationship was measured with a CHI 660E electrochemical workstation. The related biological signals involved in this article were collected from volunteers, the informed consent was obtained before the collection, and the experiments described here were conformed to the local ethical requirements.

Supporting Information

Supporting Information is available from the Wiley Online Library or from the author.

Acknowledgements

Y.G. and C.Y. contributed equally to this work. This research was financially supported by the National Natural Science Foundation of China (No. 61801403), the Independent Research Project of State Key Laboratory of Traction Power (No. 2017TPL_Z04), and the Fundamental Research Funds for the Central Universities of China (No. 2682017CX071). The authors gratefully acknowledge the Analysis and Testing Center of Southwest Jiaotong University.

Conflict of Interest

The authors declare no conflict of interest.

Keywords

microchannel confined effects, multifunctional devices, MXenes, piezoresistive sensors

Received: November 18, 2019

Revised: December 22, 2019

Published online: January 27, 2020

- [1] a) J. C. Yang, J. Mun, S. Y. Kwon, S. Park, Z. Bao, S. Park, *Adv. Mater.* **2019**, *31*, 1904765; b) X. Yu, H. Wang, X. Ning, R. Sun, H. Albadawi, M. Salomao, A. C. Silva, Y. Yu, L. Tian, A. Koh, C. M. Lee, A. Chempakasseril, P. Tian, M. Pharr, J. Yuan, Y. Huang, R. Oklu, J. A. Rogers, *Nat. Biomed. Eng.* **2018**, *2*, 165; c) G. Schwartz, B. C. Tee, J. Mei, A. L. Appleton, D. H. Kim, H. Wang, Z. Bao, *Nat. Commun.* **2013**, *4*, 1859; d) K. Meng, S. Zhao, Y. Zhou, Y. Wu, S. Zhang, Q. He, X. Wang, Z. Zhou, W. Fan, X. Tan, J. Yang, *J. Chem. Matter* **2019**, *1*, 1875; e) J. He, P. Xiao, W. Lu, J. Shi, L. Zhang, Y. Liang, C. Pan, S.-W. Kuo, T. Chen, *Nano Energy* **2019**, *59*, 422; f) C. Yan, W. Deng, L. Jin, T. Yang, Z. Wang, X. Chu, H. Su, J. Chen, W. Yang, *ACS Appl. Mater. Interfaces* **2018**, *10*, 41070.
- [2] a) W. Deng, T. Yang, L. Jin, C. Yan, H. Huang, X. Chu, Z. Wang, D. Xiong, G. Tian, Y. Gao, H. Zhang, W. Yang, *Nano Energy* **2019**, *55*, 516; b) S. Lim, D. Son, J. Kim, Y. B. Lee, J.-K. Song, S. Choi, D. J. Lee, J. H. Kim, M. Lee, T. Hyeon, D.-H. Kim, *Adv. Funct. Mater.* **2015**, *25*, 375; c) Y. C. Lai, J. Deng, R. Liu, Y. C. Hsiao, S. L. Zhang, W. Peng, H. M. Wu, X. Wang, Z. L. Wang, *Adv. Mater.* **2018**, *30*, 28.
- [3] a) C. Deng, W. Tang, L. Liu, B. Chen, M. Li, Z. L. Wang, *Adv. Funct. Mater.* **2018**, *28*, 1801606; b) G. Tian, W. L. Deng, Y. Y. Gao, D. Xiong, C. Yan, X. B. He, T. Yang, L. Jin, X. Chu, H. T. Zhang, W. Yan, W. Q. Yang, *Nano Energy* **2019**, *59*, 574; c) D. Xiong, W. Deng, G. Tian, Y. Gao, X. Chu, C. Yan, L. Jin, Y. Su, W. Yan, W. Yang, *Nanoscale* **2019**, *11*, 3021; d) Y. Guo, M. Zhong, Z. Fang, P. Wan, G. Yu, *Nano Lett.* **2019**, *19*, 1143.
- [4] a) Q. Hua, J. Sun, H. Liu, R. Bao, R. Yu, J. Zhai, C. Pan, Z. L. Wang, *Nat. Commun.* **2018**, *9*, 244; b) Z. Lou, S. Chen, L. Wang, R. Shi, L. Li, K. Jiang, D. Chen, G. Shen, *Nano Energy* **2017**, *38*, 28.
- [5] Y. Song, H. Chen, X. Chen, H. Wu, H. Guo, X. Cheng, B. Meng, H. Zhang, *Nano Energy* **2018**, *53*, 189.
- [6] K. Xia, C. Wang, M. Jian, Q. Wang, Y. Zhang, *Nano Res.* **2018**, *11*, 1124.
- [7] a) J. Lee, S. Pyo, D. S. Kwon, E. Jo, W. Kim, J. Kim, *Small* **2019**, *15*, 12; b) Y. Cai, J. Shen, G. Ge, Y. Zhang, W. Jin, W. Huang, J. Shao, J. Yang, X. Dong, *ACS Nano* **2018**, *12*, 56.
- [8] Y. Zhu, J. Li, H. Cai, Y. Wu, H. Ding, N. Pan, X. Wang, *Sens. Actuators, B* **2018**, *255*, 1262.
- [9] a) Q. J. Sun, J. Zhuang, S. Venkatesh, Y. Zhou, S. T. Han, W. Wu, K. W. Kong, W. J. Li, X. Chen, R. K. Y. Li, V. A. L. Roy, *ACS Appl. Mater. Interfaces* **2018**, *10*, 4086; b) H. Li, K. Wu, Z. Xu, Z. Wang, Y. Meng, L. Li, *ACS Appl. Mater. Interfaces* **2018**, *10*, 20826; c) T. Li, L. Li, H. Sun, Y. Xu, X. Wang, H. Luo, Z. Liu, T. Zhang, *Adv. Sci.* **2017**, *4*, 1600404.
- [10] C. Lang, J. Fang, H. Shao, X. Ding, T. Lin, *Nat. Commun.* **2016**, *7*, 11108.
- [11] a) K. Dong, Z. Wu, J. Deng, A. C. Wang, H. Zou, C. Chen, D. Hu, B. Gu, B. Sun, Z. L. Wang, *Adv. Mater.* **2018**, *30*, 43; b) C. Yan, Y. Gao, S. Zhao, S. Zhang, Y. Zhou, W. Deng, Z. Li, G. Jiang, L. Jin, G. Tian, T. Yang, X. Chu, D. Xiong, Z. Wang, Y. Li, W. Yang, J. Chen, *Nano Energy* **2019**, *67*, 104235.
- [12] a) T. Li, L. Li, Y. Bai, Y. Cao, Q. Lu, Y. Li, G. Xu, T. Zhang, *Nanoscale* **2019**, *11*, 5737; b) L. Pan, A. Chortos, G. Yu, Y. Wang, S. Isaacson, R. Allen, Y. Shi, R. Dauskardt, Z. Bao, *Nat. Commun.* **2014**, *5*, 3002; c) Y. Wan, Z. Qiu, J. Huang, J. Yang, Q. Wang, P. Lu, J. Yang, J. Zhang, S. Huang, Z. Wu, C. F. Guo, *Small* **2018**, *14*, 1801657; d) A. dos Santos, N. Pinela, P. Alves, R. Santos, E. Fortunato, R. Martins, H. Águas, R. Igreja, *Adv. Electron. Mater.* **2018**, *4*, 1800182.
- [13] J. Shi, L. Wang, Z. Dai, L. Zhao, M. Du, H. Li, Y. Fang, *Small* **2018**, *14*, 1800819.
- [14] Z. Wang, S. Wang, J. Zeng, X. Ren, A. J. Chee, B. Y. Yiu, W. C. Chung, Y. Yang, A. C. Yu, R. C. Roberts, A. C. Tsang, K. W. Chow, P. K. Chan, *Small* **2016**, *12*, 3827.
- [15] Y. Pang, K. N. Zhang, Z. Yang, S. Jiang, Z. Y. Ju, Y. X. Li, X. F. Wang, D. Y. Wang, M. Q. Jian, Y. Y. Zhang, R. R. Liang, H. Tian, Y. Yang, T. L. Ren, *ACS Nano* **2018**, *12*, 2346.
- [16] B. H. Zou, Y. Y. Chen, Y. H. Liu, R. J. Xie, Q. J. Du, T. Zhang, Y. Shen, B. Zheng, S. Li, J. S. Wu, W. N. Zhang, W. Huang, X. Huang, F. W. Huo, *Adv. Sci.* **2019**, *6*, 1801283.
- [17] Z. Lou, S. Chen, L. Wang, K. Jiang, G. Shen, *Nano Energy* **2016**, *23*, 7.
- [18] Q. Wang, M. Jian, C. Wang, Y. Zhang, *Adv. Funct. Mater.* **2017**, *27*, 1605657.
- [19] a) A. Sarycheva, A. Polemi, Y. Liu, K. Dandekar, B. Anasori, Y. Gogotsi, *Sci. Adv.* **2018**, *4*, eaau0920; b) D. Xiong, X. Li, Z. Bai, S. Lu, *Small* **2018**, *14*, 1703419; c) B. Anasori, M. R. Lukatskaya, Y. Gogotsi, *Nat. Rev. Mater.* **2017**, *2*, 16098; d) Z. Ling, C. E. Ren, M. Q. Zhao, J. Yang, J. M. Giannarico, J. Qiu, M. W. Barsoum, Y. Gogotsi, *Proc. Natl. Acad. Sci. U. S. A.* **2014**, *111*, 16676.
- [20] Y. Ma, N. Liu, L. Li, X. Hu, Z. Zou, J. Wang, S. Luo, Y. Gao, *Nat. Commun.* **2017**, *8*, 1207.
- [21] a) K. Wang, Z. Lou, L. Wang, L. Zhao, S. Zhao, D. Wang, W. Han, K. Jiang, G. Shen, *ACS Nano* **2019**, *13*, 9139; b) Z. Chen, Y. Hu, H. Zhuo, L. Liu, S. Jing, L. Zhong, X. Peng, R.-c. Sun, *Chem. Mater.* **2019**, *31*, 3301.
- [22] L. Zhao, F. Qiang, S. W. Dai, S. C. Shen, Y. Z. Huang, N. J. Huang, G. D. Zhang, L. Z. Guan, J. F. Gao, Y. H. Song, L. C. Tang, *Nanoscale* **2019**, *11*, 10229.